Project: "Synthesis, Characterization and Testing of Hydrogen Permeation Barriers (HPBs) applied as a safety measure for future fusion reactors"

Project type: Post-doctoral research

Project registration code: PN-III-P1-1.1-PD-2019-0745

Project acronym: SCTHPB

Summary of final scientific and technical report,

Following, notable results (summarized version) are presented and discussed in relation to the main objectives included in the primary project proposal.

Objective I. Deposition of hydrogen permeation barriers

The synthesis of layers with effective properties for reducing the permeation of hydrogen isotopes in metallic walls with relevance in the field of nuclear fusion was pursued. Synthesis activities were implemented through which the deposition of thin layers of materials known in the literature was realized, both in pure depositions and co-depositions aiming to exploit the possibility of determining new layers with improved barrier properties of permeation. At the same time, the aim was to establish feasible configurations adapted to each individual deposition method, optimizing the deposition parameters and streamlining the process itself.

Thus, in order to achieve the objective proposed in the project, metal, oxide and oxide-metal alloy coatings were made by applying different plasma deposition techniques existing in the research infrastructure as well as in industry (table 1).

Table 1. Deposited configurations and their associated methods;

Methods	Configurations (substrates)		
	Metallic depositions	Oxides	Co-depositions
TVA	W(Al, SS); Be (Al, SS);	-	W:Be (Al, SS,V, Zr);
CMSII	W (Al, SS, V, Zr);	-	-
HIPIMS	-	SiO_2(Al, SS),Cr_2O_3(Al, SS),Al_2O_3(Al, SS),Er_2O_3(Al, SS)	-
RF / DC magnetron	-	SiO_2(Al, SS),Cr_2O_3(Al, SS),Al_2O_3(Al, SS),Er_2O_3(Al, SS)	W/[SiO_2(Al), Cr_2O_3(Al), Al_2O_3(Al), Er_2O_3(Al)]; Be/[SiO_2(Al), Cr_2O_3(Al), Al_2O_3(Al), Er_2O_3(Al)]
AP	W(Al, SS);	Cr_2O_3(Al, SS);Er_2O_3(Al, SS); Al_2O_3(Al, SS);Al_2O_3+TiO_2(Al, SS)	-

Objective II Microstructural, morphological, chemical and mechanical investigations on deposited layers

For the present objective, the depositions of metals (W, Be, W:Be), oxides (Al_2O_3, Cr_2O_3, Er_2O_3 and SiO_2) and metal-oxides (W/Be: Al_2O_3, Cr_2O_3, Er_2O_3 and SiO_2) carried out within the project by the techniques that consisted of the thermionic arc in vacuum (TVA), magnetron (CMSII, RF- radio frequency, DC- direct current) and metallization (plasma jet) were investigated according to the structural parameters (morphology, adhesion, hardness, desorption) in order to validate the deposits and candidate configurations for their inclusion in future permeation measurements. The main motivation consisted in the fact that the morphology of the surface influences the relevant parameters such as solubility, diffusion and last but not least the permeation through the deposited layer. Therefore, the applicability of deposits as permeation barriers can be estimated by performing complex analyzes on the surface morphology, strongly influenced by the chemical and physical structure of the deposits. Thus, a selection of samples was made based on the determined measurements.

In order to study the surface morphology and the micro-analysis of the stoichiometry composition, methods such as scanning electron microscopy (SEM) and energy dispersive X-ray spectroscopy (EDX) were applied. The relevant parameters such as the roughness and hardness of the deposited films were studied by atomic force microscopy (AFM) and indentation. Calibration of deposition rates and film thickness was performed by cross-sectional SEM analysis. Additionally, alternative thickness validation methods such as the X-ray fluorescence technique (XRF) and compositional analysis in depth by optical emission spectroscopy (GDOES) were applied. The structural integrity at the micrometric level was achieved by the X-ray laminography (XCL) technique, so that the deposited layer and the film-substrate interface were followed. The desorption study, which determined the presence of adsorbed gases on the surface and in the film structures, was carried out by thermal desorption spectroscopy (TDS). Therefore, by studying the morphology, chemical structure and mechanical properties of the deposited layers, films were validated in the permeation measurements included in the next stage of the project.

2.1 Morphological and compositional characterization by SEM, EDX, GDOES, XPS and XRF on selected sample

2.1.1 Morphological characterization by SEM

Following the surface analysis by the SEM technique (figure 2.1 and 2.2), differences were observed depending on the configurations of the studied films, namely: high roughness with deep delamination and conglomerates with random orientations (Cr_2O_3, Er_2O_3, Al_2O_3:Be); random nucleation's with growth of conical structures (Cr_2O_3:W) and granularity (Cr_2O_3:Be); smooth surfaces without defined particularities (SiO_2, Er_2O_3:W, Al_2O_3:W); isolated artifacts (SiO_2:W, Er_2O_3:Be, Al_2O_3); high roughness with cavity type defects (SiO_2:Be);

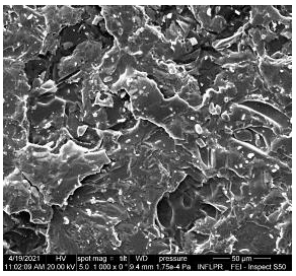

(a) Cr_2O_3

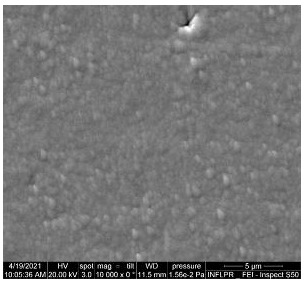

(b) Cr_2O_3 : W

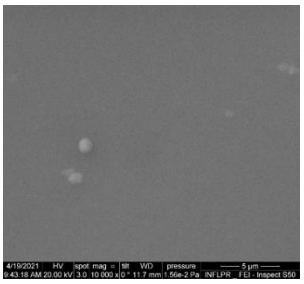

(c) Cr_2O_3 : Be

Figure 2.1 SEM images magnified x 5 ~10k; Deposited samples by HIPIMS with configuration: (a) Cr_2O_3; (b) Cr_2O_3 : W; (c) Cr_2O_3 : Be;

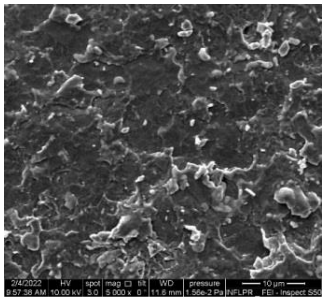

(a) Cr_2O_3

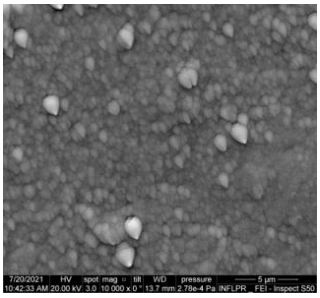

(b) Cr_2O_3 : W

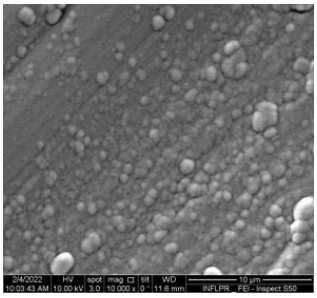

(c) Cr_2O_3 : Be

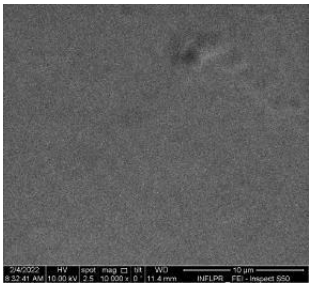

(d) Al_2O_3

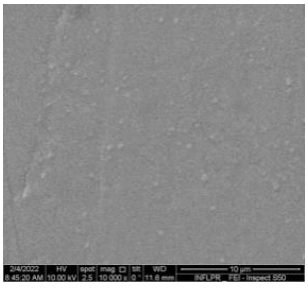

(e) Al_2O_3 : W

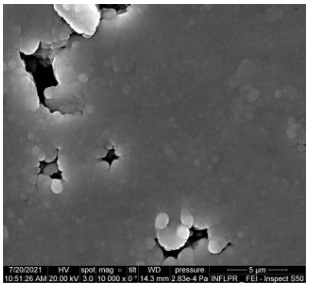

(f) Al_2O_3 : Be

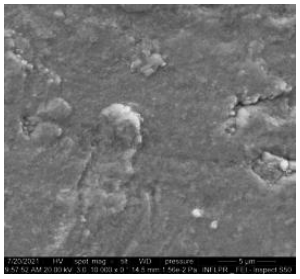

(g) Er_2O_3

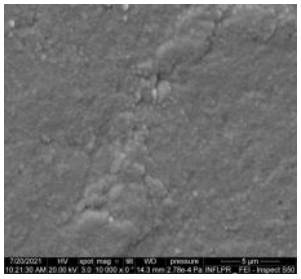

(h) Er_2O_3 : W

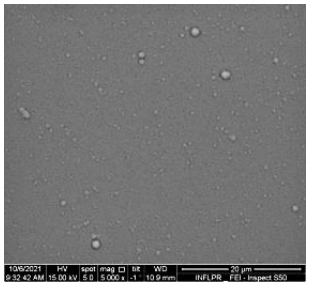

(i) Er_2O_3 : Be

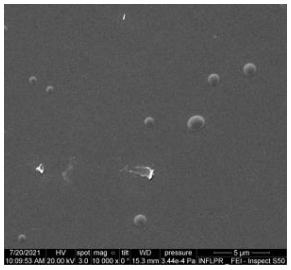

(j) SiO_2

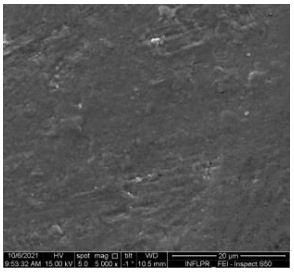

(k) SiO_2 : W

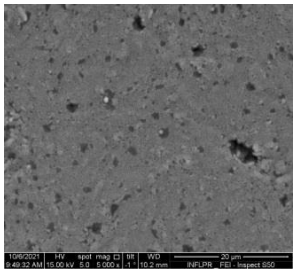

(l) SiO_2 : Be

Figure 2.2 SEM on samples deposited on RF/DC magnetron with following configurations: (a) Cr_2O_3; (b) Cr_2O_3 : W; (c) Cr_2O_3 : Be; (d) Al_2O_3; (e) Al_2O_3 : W; (f) Al_2O_3 : Be; (g) Er_2O_3; (h) Er_2O_3 : W; (i) Er_2O_3 : Be; (j) SiO_2; (k) SiO_2 : W; (l) SiO_2 : Be;

Through SEM images, it was possible to determine the change in the surface morphology of Cr_2O_3 and SiO_2 oxides, while artifacts such as nucleation were observed for SiO_2:Be. Compared to the co-depositions with Be, those with W have a decreasing impact on the roughness factor (RMS) determined by the post-processing and interpretations made on the AFM results (figure 2.3).

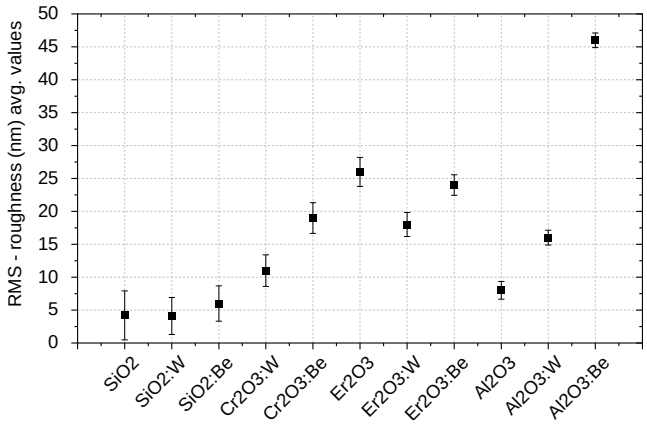

Figure 2.3 Determined values for the RMS value;

Also, the morphology and roughness of the films was evaluated by AFM. The AFM measurements and the values of the roughness parameter (RMS) contributed to obtaining important information regarding the morphology of the pure oxide layers and the metal oxide configurations. Therefore, the configurations that involved Er_2O_3 determined a morphology with mixed granularity, while the presence of Be determined the increase of granularity, respectively of the RMS parameter. This result was also confirmed by the surface SEM images on the Er_2O_3:Be configuration showing artifacts compared to the pure oxide which has a smooth surface. The presence of Be in the configurations with Er_2O_3 and SiO_2 determined an increase of more than (50%) of the RMS parameter. Also, in the case of these oxides, it was observed that W causes a homogenization of the layer surface, while Be forms isolated nucleation, thus causing the appearance of artifacts confirmed by the SEM technique. Different results could be observed in the case of Cr_2O_3, through delamination type structures, these being reduced by co-depositions with W and Be. The smallest variation of the RMS factor was observed in the case of co-depositions involving Al_2O_3, while the SEM images showed a smooth and uniform surface with isolated cone-shaped areas, a fact also observed by surface investigations by AFM.

Instead, the SEM images acquired on the samples deposited by the AP method highlighted the presence of defects (cracks, non-deposited areas, delamination, etc.), exemplified in figure 2.4. Thus, the AP submissions could not be validated as defect-free layers.

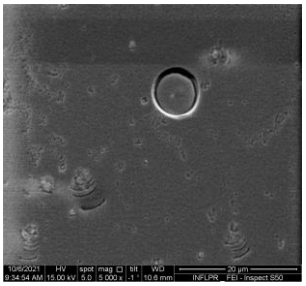

(a) Er_2O_3

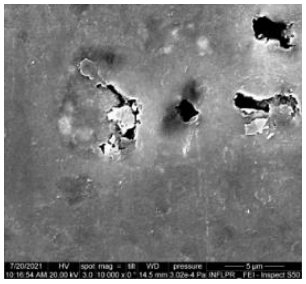

(b) Cr_2O_3

Figure 2.4. SEM images on AP-plasma deposited configurations: (a) Er_2O_3; (b) Cr_2O_3;

The measurements on the metal samples submitted by TVA revealed homogeneous layers for Be:W (figure 2.5.b), as well as compact layers for W (figure 2.5.c), without the presence of defects.

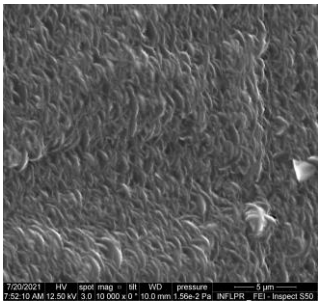

(a) Be

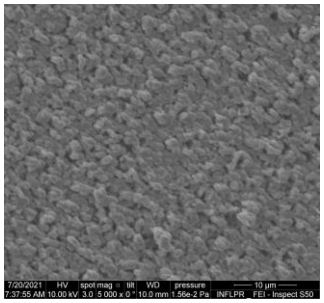

(b) Be:W

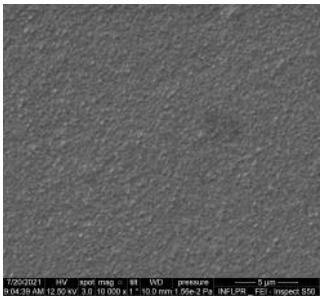

(c) W

Figure 2.5. SEM images of TVA deposited samples: (a) Be, (b) Be:W and (c) W;

Thus, it was determined that the layers of W, Be (deposited by TVA) and respectively Al_2O_3 (deposited by RF magnetron) present compact and defect-free surfaces.

2.1.2 Compositional analysis EDX

The elemental analysis was carried out by the EDX technique integrated in the SEM instrument. The oxygen concentration study was performed on the configurations deposited by the RF/DC magnetron deposition method. The results thus determined indicated an O content (wt.%) at values close to the ratio of the stoichiometric configuration, confirming the existence of the oxide-metal configuration in the analyzed films. Except for the configurations containing Be (SiO_2:Be, Er_2O_3:Be and Al_2O_3:Be), EDX measurements determined that the oxides (Cr_2O_3, SiO_2, Al_2O_3, Er_2O_3) contain O (wt.%) at values close to the proposed atomic ratio in the stoichiometric configuration, while the existence of the metal-oxide state was confirmed for the samples Er_2O_3:W and Al_2O_3:W.

2.1.3 Surface chemical analysis by X-ray photoelectron spectroscopy (XPS)

XPS measurements were made to determine the bonding state of surface atoms and then quantitative analysis and relative chemical state concentrations were performed. Thus, the spectra of the bonding states of the corresponding atoms were investigated for the co-depositions of metal-oxides, depositions made by DC/RF magnetron, characterizing the layers as a mixture of oxidized metals. Narrow XPS spectra of the photoelectron lines were recorded to determine the chemical changes at the surface of

the Al, Er, Si and Cr systems on a total of 12 configurations. Notably for all the studied systems, it was observed that due to the affinity of Be to oxygen, it can protect the co-deposited layer against the oxidative process.

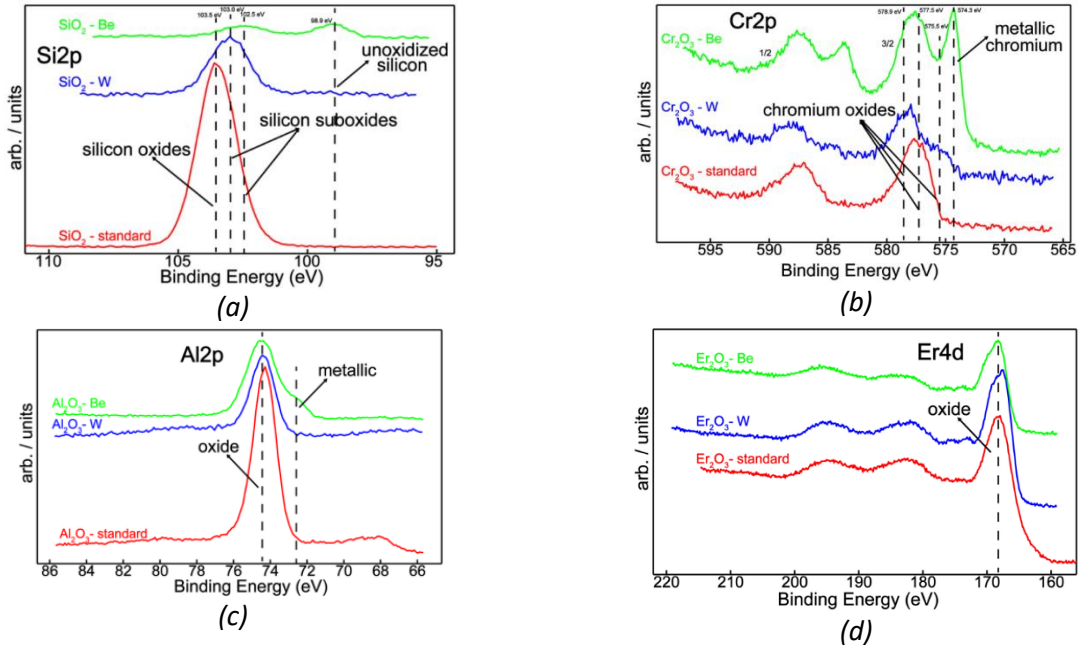

Figure 2.6. XPS spectra for the studied configurations: (a) Si2p line for SiO_2; (b) Cr2p line on Cr_2O_3configuration; (c) Al2p line for Al_2O_3 configuration; (d) Er4d line for Er_2O_3 [1];

The chemical behavior of Si in relation to the addition of Be and W indicated an increase in its binding energy from 98.9 to 103.5 eV. This means that there is a gradual oxidation process of silicon on the surface of the sample in the presence of Be and W atoms. Moreover, by integrating the Si2p energy peak, the oxidation state of the Si samples could be identified. The energy peaks located at 98.9 eV and 1035 eV are attributed to the unoxidized state of Si, respectively completely oxidized thus forming SiO_2. The two underoxidized states of Si at 102.5 eV and 103.0 eV can be associated with stoichiometry x between 1.2-1.6 and 1.5-1.9 respectively (figure 2.6.a). Visual inspection of the aluminum films showed constant chemical behavior at higher binding energies of the relevant Al2p photoemission, suggesting the formation of Al_2O_3 at 74.4 eV (figure 2.6.b) [2, 3]. The only determining chemical change among the samples containing Al represents the formation of metallic aluminum which is associated with the presence of Be. This fact is validated by the integration of the Al2p energy spectrum. As a result, the features identified at 72.7 eV and 74.4 eV (figure 2.6.c) can be attributed to unoxidized Al [2, 3] and Al_2O_3 [2, 3]. This particular behavior can be explained by considering the strong chemical affinity of Be for oxygen, thus protecting aluminum against oxidations. Similar chemical behavior could be observed for erbium (figure 2.6.d). The superimposed spectrum for Er4d indicated an oxidized surface of Er, forming Er2O3, identified in the spectrum by the presence of the 168.6 eV peak, with multiple associated spectral peculiarities [4, 5].

2.2 Volumetric (XCT), structural (XRD) and desorption (TDS) studies; Mechanical studied by micro-indentation;

2.2.1 Volumetric studied by X-ray laminography (XCL)

Studies were carried out in order to carry out multiscale investigations at the facility developed within the INFLPR [6]. This objective envisioned the validation of high-purity, dense, artifact-free layer depositions at a resolution of up to 3 µm. Volumetric measurements performed by X-ray laminography (XCL) contributed to a non-destructive analysis in volume on the structural integrity of the analyzed layers as an alternative to surface imaging by SEM, providing information on the presence of pores and cracks in the thick deposits, as well as the interface between deposition and substrate.

The selection of samples for XCL measurements was carried out by analyzing 2D radiographic images (10µm/pixel), thus looking at the preliminary determination of structural integrity. In general, the samples deposited by magnetron had quasi-homogeneous structures, the exception being in the case of Cr2O3 deposits deposited by RF magnetron, respectively W deposited by the CMSII method (figure 2.7). The nonlinear profiles associated with the gray levels extracted from the radiographic images showed a strong variation especially for the Cr2O3 sample.

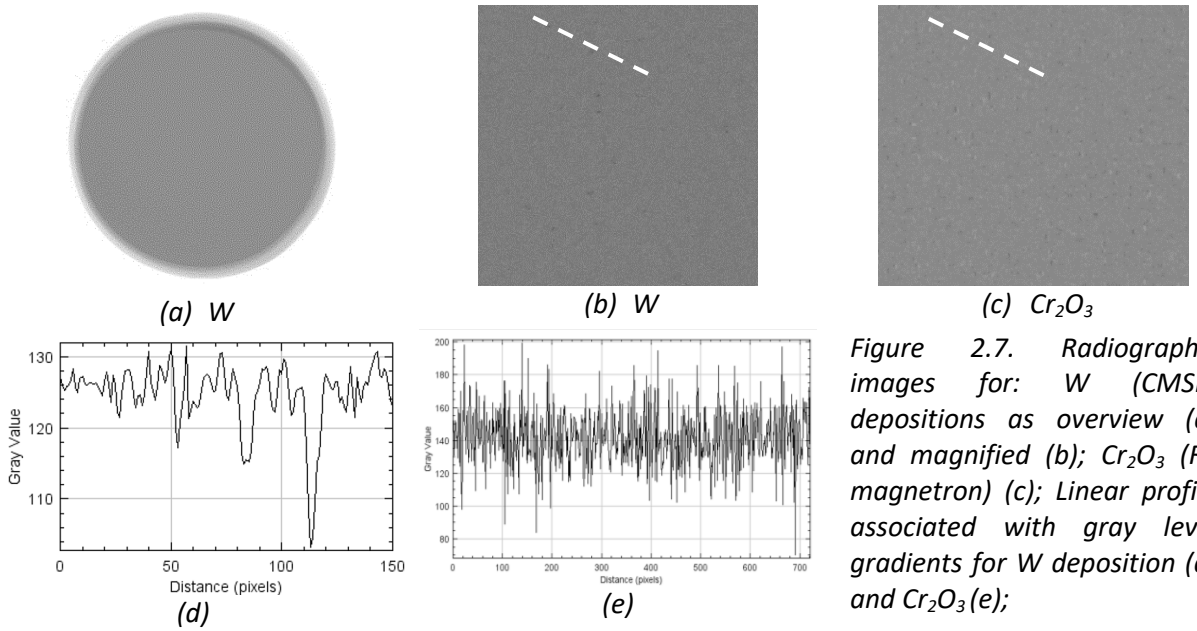

(a) W *(b) W* *(c) Cr_2O_3*

(d) *(e)*

Figure 2.7. Radiographic images for: W (CMSII) depositions as overview (a) and magnified (b); Cr_2O_3 (RF magnetron) (c); Linear profile associated with gray level gradients for W deposition (d) and Cr_2O_3 (e);

For the W sample that demonstrated notable artifacts in the radiographs, an X-ray tomography (XCT) measurement was performed in a laminography (XCL) configuration, in order to determine the presence of defects in the form of pores in the volume or at the interface with the substrate (Si) which is completely transparent to X-rays. In figure 2.8, the presence of pores in the volume of the layer was highlighted in the 3D reconstruction, these being completely embedded and not identified by SEM imaging. Thus, the presence of pores on the W configuration deposited by the magnetron sputtering technique (CMSII) was determined, both at the surface level and at the interface between the layer and the substrate. Thus, there were determined pores perpendicular to the substrate and which represent communicating paths that would considerably decrease the permeability property of the layer, parallel cracks that could cause delamination, as well as pores determined in volume and identified at the interface with the substrate. The appearance of pores at the interface with the substrate could be explained by the desorption of gases from the Si substrate during the magnetron plasma deposition process.

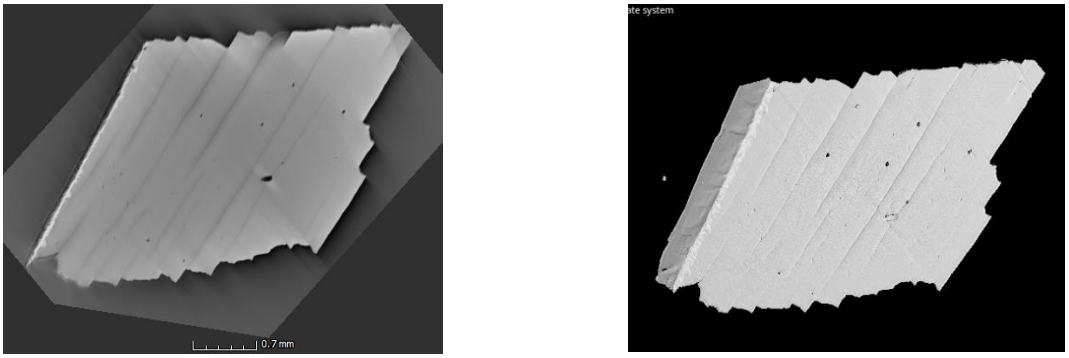

(a) (b)

Figure 2.8. Pores and multiple cracks perpendicular to the substrate were observed on the deposition of W on Si; (a) – section at the interface between substrate and layer with the appearance of additional pores compared to those visualized by 3D rendering (b);

2.2.2. X-ray diffraction (XRD) analysis

The XRD characterization of Cr_2O_3, Cr_2O_3:W, SiO_2 and SiO_2:W samples is presented in figure 2.9. Cr_2O_3 and SiO_2 deposition on graphite (ICDD 04-014-0362) showed amorphous phases without specific structures, a result usually found on oxides deposited by magnetron sputtering at room temperature [7, 8].

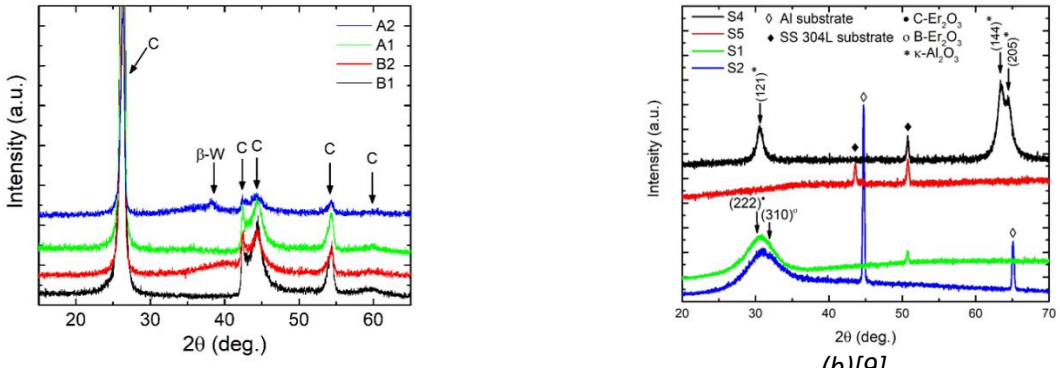

(a)[1] *(b)[9]*

Figure 2.9. XRD analysis on magnetron deposited configuration: Er_2O_3 (a), Al_2O_3 (a), SiO_2 (b) and Cr_2O_3 (b);

For the Cr_2O_3:W sample, the β-W phase (ICDD 00-047-1319) was observed in the XRD spectra, but the peak corresponding to the (210) diffraction phase has a low intensity and with a 2θ position shift which indicates formation of distorted structures. Also, the SiO_2:W sample presents the β-W phase through the intensity peak centered around 2θ=39.85°, suggesting a short coherence length resulting from the order of the structural planes at small distances.

The contribution of the substrates in the XRD spectra was determined as narrow spectral peaks. In the case of Er_2O_3 and Er_2O_3:W samples, spectral peaks corresponding to Er_2O_3 in the stable cubic phase (ICDD 04-008-8242) and the metastable monoclinic face (ICDD 04-016-5846) were observed. Also, the contribution of the Er metal layer (ICDD 01-082-3299) can be associated with the presence of Er_2O_3. References [10, 11] suggest the coexistence of two phase states for Er_2O_3 when the samples are

deposited on the substrate at a temperature lower than 600°C, and the bias voltage did not significantly change the stability of the monoclinic system.

For the Al_2O_3 sample system, the metastable crystalline phase κ-Al_2O_3 (ICDD 00-052-0803) is highlighted and was previously reported in [10, 11], where the formation of this phase is favored on certain substrates and deposition conditions. In comparison, no diffraction peak for the Al_2O_3:W system was observed. In addition, the addition of W disturbs the stability of κ-Al_2O_3, but has no influence on the structure of the sample. It is notable that the deposition of κ-Al_2O_3 exerts a good mechanical and anti-erosion property that can be favorable in the protection of surfaces, and despite the metastable nature of κ-Al_2O_3, the transition to stable phases occurs at very high temperatures [12]. Moreover, in these polycrystalline systems with significant structural disorder, the discrete peaks show a displacement from the central position due to the small values of the coherence length and the considerable mechanical stress between the crystallographic planes.

2.2.3 Thermal desorption studies (TDS)

The TDS measurements were carried out in order to evaluate the degassing process of the atomic species integrated in the matrix of the deposited elements. To perform desorption measurements and study elements such as H_2O (18), N_2 (28), O_2 (32), CO_2 (44), the configurations deposited on silicon and carbon were placed in an oven with a heating ramp of 10° C/min, thus following the desorption differences at the specific temperatures in accordance with the connecting forces between the elements and with the structural cavities.

The TDS spectra for the sample Er_2O_3 (figure 2.10.a) showed a constant desorption of water, and the threshold of 300°C marks the appearance of elements with stable bonds N_2, CO_2, and O_2. The sample Er_2O_3:Be (figure 2.10.b), represents a different retention behavior, while the lack of O_2 and the low retention of H_2O whose desorption can be observed after the temperature of 500°C can be observed, a fact associated with the presence of structural traps.

No difference in H_2O desorption mechanisms was observed for the Al_2O_3 configurations, while the presence of W or Be significantly reduced the recorded signal. The notable difference between the two configurations consists in the fact that N2 desorption takes place at different temperatures such as 500°C in the case of co-deposition with Be and 800°C respectively for co-deposition with W.

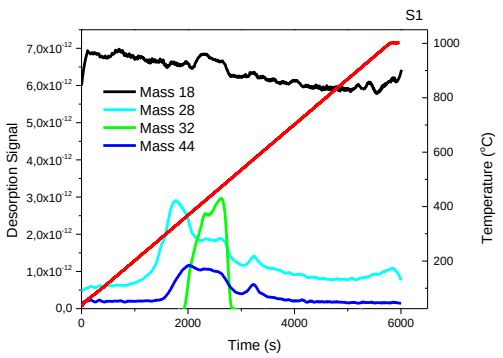

(a) Er_2O_3

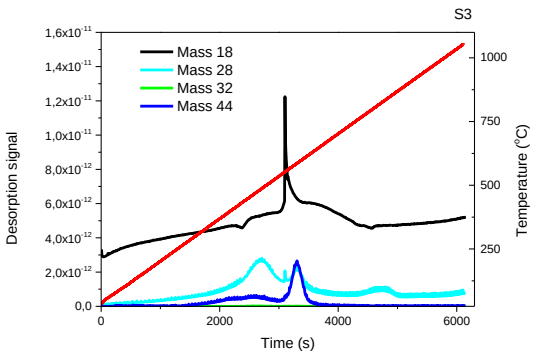

(b) Er_2O_3:Be

Figura 2.10. Example of TDS spectra realized at a heat treatment with a temperature ramp of 10 °C/min for Er_2O_3 (a), Er_2O_3:Be (b); Er_2O_3:W was fully delaminated after the heat treatment;

Significant desorption for H_2O (at 400 °C) was observed for the Cr_2O_3 sample. In general, CO_2 desorption could be observed at similar temperatures for all configurations studied. Large variations of N_2 as a function of temperature for the studied configurations were observed: quasi-linear increase in relation to Cr_2O_3; strongest signal at maximum applied temperature for Cr_2O_3:W; Strong signal recorded at 400°C for co-depositions containing Be (eg Cr_2O_3:Be and SiO_2:Be).
The raw TDS spectra suggest the presence of the oxidation state on the surface that determined the desorption of N_2 at high temperatures [13], the exception being SiO_2:Be, results consistent with those determined by the EDX method. For the signature of O_2, no notable differences were recorded, a signal close to the background signal predominating (figure 2.10).

2.2.4 Mechanical proprieties

The indentation hardness (HIT), the indentation modulus (EIT) and the relative deformation expressed by the H/E ratio were determined. The H/E ratio provides information relevant to the tribometric measurements on the 12 configurations deposited by RF/DC magnetron. According to the literature [14], a deposit with high HIT and low EIT values shows improved mechanical properties with a low friction coefficient in tribometric measurements. As a result, the Al_2O_3 sample was determined to have a higher resistance to wear and tear, compared to the other configurations studied (figure 2.11.a).

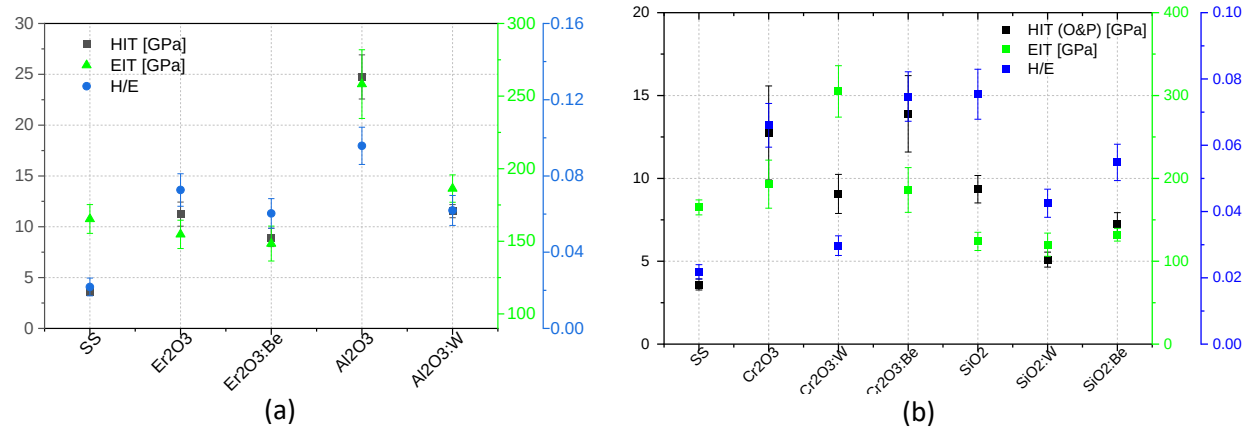

Figure 2.11. The indentation hardness (HIT), the indentation modulus (EIT) and the relative deformation expressed by the H/E ratio for the systems deposited on SS substrates: (a) Al_2O_3, Er_2O_3 (b) SiO_2 and Cr_2O_3;

The Al_2O_3:Be configuration expressed a high hardness; SiO_2:W expressed small values, and in general, Cr_2O_3 is harder than SiO_2, an observation also reported in other works [15]. Also, W co-deposited with oxides tends to significantly influence the properties of the films by decreasing the hardness by a factor of 2, while Be shows a high probability for increasing the average hardness by a factor of 2.

Objective 3 Deposition characterizations by permeability, thermal conductivity and hardness

3.1 Coatings validation by thermal treatments exposure

The thermal treatments were carried out before the measurements relevant to the mechanical properties such as micro-hardness and adhesion.

The exposures to thermal treatments of the samples were carried out in the same premises where the TDS measurements were made, applying a heating ramp of 10 °C/min, up to a maximum temperature of 1000 °C and a maximum time of 2 hours . The validation of the deposits was sought by investigating their delamination/exfoliation behavior, and to accentuate the weak adhesion effect, the use of samples deposited on Si (10 × 10 mm^2) with a low roughness was chosen [16].

Following the measurements applied to the samples deposited by magnetron in RF/DC mode, the configurations Cr_2O_3:Be and Er_2O_3:W were determined as having a high probability of exfoliation due to thermal treatments. However, in order to perform the TDS measurements on all the proposed configurations, the thermal treatments were repeated on the two configurations having C substrate, which eliminated the delamination behavior, because the surface morphology of the C substrate shows an increased roughness and helps to improve adhesion from during the submission process.

3.2 Characterization of the layers in terms of permeability by validating them as hydrogen isotope permeation barriers

The H_2 permeation measurements were aimed at determining the permeation reduction factor (PRF) through the layer and validating the deposited layers as permeation barriers. The specific conditions of the permeation measurements required the strict selection of configurations with relevant properties. In choosing the configurations of the deposits, the results obtained from the morphological, structural and mechanical studies were taken into account, which determined the configurations determined to be dense, without macroscopic defects and with isotropic structures.

The permeation measurements were made on selected deposits (W / 304L, Al2O3 / 304L, Be / 304L) and on the reference substrate (304L). The hydrogen permeation rate (J) was quantified by the "pressure-rise" method. This method consisted in monitoring the H2 pressure accumulated over time in a calibrated volume (downstream, >1µbar) following the transfer of the gas from the pressurized enclosure (upstream, ~860 mbar) through the studied samples, the sample itself acting as a membrane between the two charms. The permeation measurements were performed at a constant temperature of 400°C, and the enclosure volume was 0.458 L.

The measurement conditions consisting of the working temperature, the advanced vacuum in both enclosures have a considerable influence on the precision with which the increase in pressure is recorded as a function of time. Therefore, in the calibration stage, mass spectroscopy measurements were made, which were further used in the application of Sievert's law [17] from the equation:

$$J = -\frac{P}{d}p^{1/2} \quad (1)$$

where P is the permeability, d represents the thickness of the studied layer and p the pressure in the upstream enclosure. These consisted in the detection of the mass of hydrogen by mass spectrometry at different upstream pressures (186 ~ 975mbar). The currents recorded by the mass spectrometer for H_2

were monitored. The data were extracted, and the values correspond to the average values in the interval in which H_2 stabilized (figure 3.1.a). In addition, mass 18 (H_2O) was monitored as a background signal, as well as the gradual decrease in pressure in the upstream area, starting from 186 mbar until it reaches 179 mbar, after which a stabilization of the H2 signal is observed. After the same procedure was applied for each pressure, then the graph of the dependence of the current signal as a function of pressure was determined (figure 3.1.b).

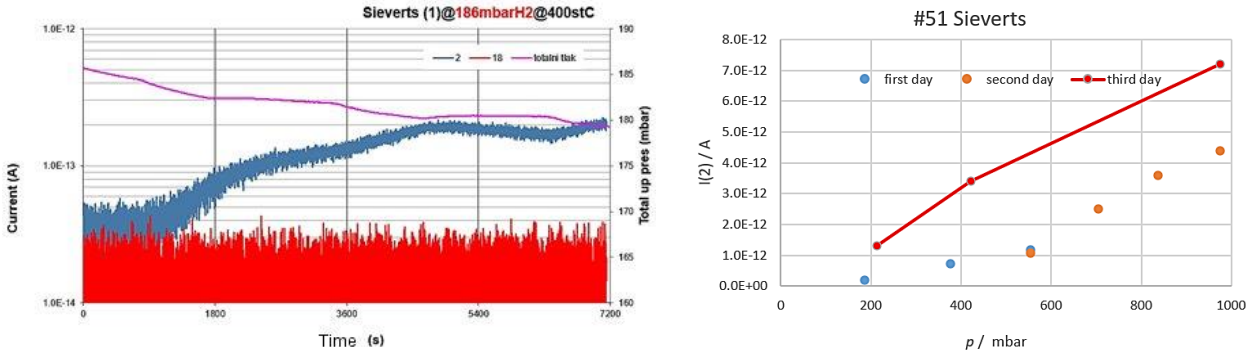

(a) (b)

Figure 3.1 (a) Effective current in relation to unit time for H_2 and H_2O; (b) Effective current for H_2 expressed as a function of the pressure at which the measurements were made.

As a result, the downstream pressure increase measurements (figure 3.2) were performed on the SS substrate (304L), to determine a background signal and compare the determined values with those previously reported in the literature.

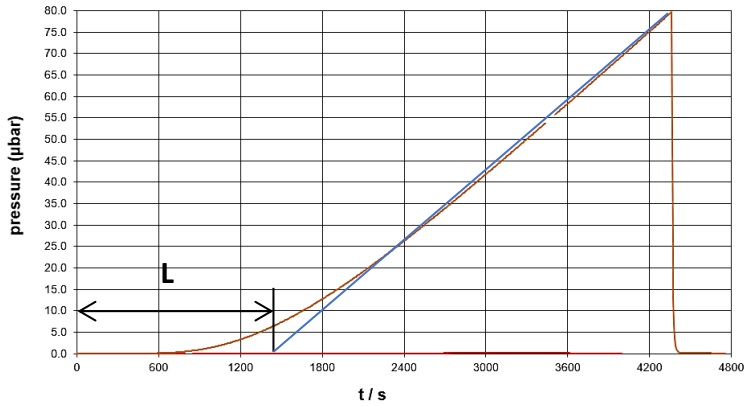

Figure 3.2. The pressure rise curve in relation to time, expressed for the SS membrane (304L);

From the graph of the dependence of "downstream" pressure (µbar) as a function of time (s), the slope of the curve and the latency time (L) were extracted, which represents the time traveled until the intersection with the asymptote of the curve. Having determined the slope and the latency time, the diffusivity (D) of the material can be determined by the formula:

$$L = \frac{d^2}{6D} \tag{2}$$

where d is the thickness of the studied membrane [18]. Thus, the diffusion and the permeation coefficient (figure 3.3) for SS were determined and were compared with the data previously reported in the literature [19]. The values determined for the diffusion are in accordance with those reported in the literature, instead, the permeation coefficient was a high one, important to consider for the calculation of the PRF for the measurements made in the present case.

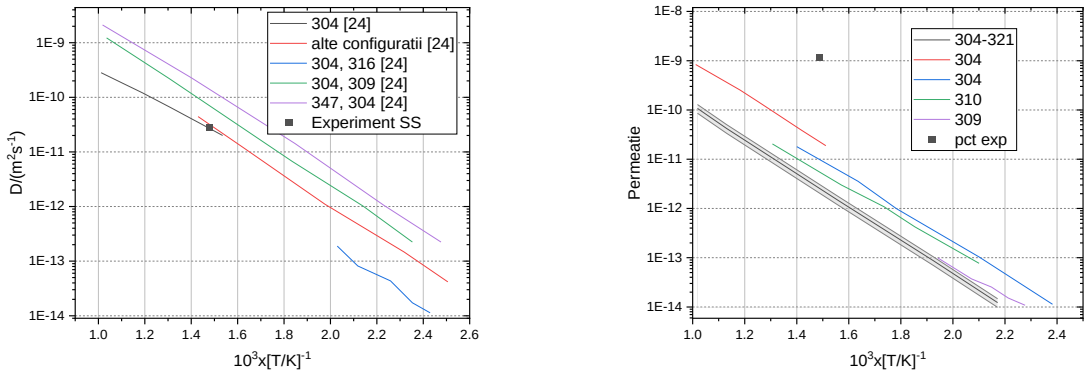

(a) (b)

Figure 3.3. Determination of the diffusion coefficient (a) and permeation (b) for the SS substrate;

The same graph of "downstream" pressure dependence (µbar) as a function of time (s) was recorded for Al_2O_3, W and Be (figure 3.4), subsequently extracting the slope of the curve and the latency time (L).

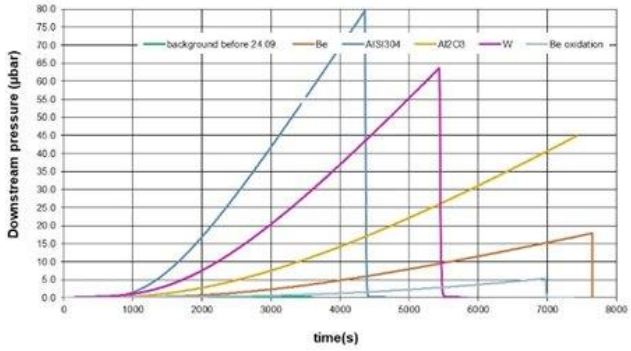

Figure 3.4. Pressure rise with time in „downstream" chamber;

Following these measurements, the permeation reduction factor (PRF) was determined for W / 304L, 304L (substrate only), Al_2O_3, Be / 304 (table 3.1). And the main goal was to validate the operating parameters of the deposition methods used in the present case (Vacuum Thermionic Arc for metal samples and RF magnetron sputtering for oxide).

Table 3.1. Permeation reduction factor for studied configurations (PRF)

Sample	Thickness [µm]	L (s)	P ($x10^{-15}$ mol H_2/(m s $Pa^{0.5}$)]	D(m^2/s) * 1E-11	PRF
W	5	1750	4.1	9.5	3.7

Be	5	1250	3.1	1.3	2.8
Al_2O_3	2	2500	2.3	6.6	2.1

3.3.2 Mechanical properties (micro-hardness, adherence)

Results determined from Vickers hardness measurements with micro loads (Vickers micro hardness) were presented in figure 3.5. Here we mention the fact that the results can be influenced by the measurement conditions, the accuracy of the reading of the diagonals being limited by the resolution of ± 0.1 μm, of the trace left by the indentation tip, the topology and the thickness of the analyzed samples. Taking into account the influence of the substrate that could affect the results, and given the fact that the depth to which the indentation occurs is greater than 10% of the thickness of the deposit, the changes in the hardness of the deposits had the SS substrate as a reference. The trace left by the indenter defined by D and the thickness T of the studied material must satisfy the requirement D<T [20], thus avoiding the "cold flow effect" phenomenon. For a Vickers indenter, D can be expressed as D=d/7, where d represents the average value of the diagonal print. For all the samples studied, this condition was satisfied. Furthermore, up to 10 measurements per sample were performed at different locations on the sample surface, and the results are expressed as mean values and the deviation represented by the standard deviation.
The maximum hardness value was obtained for the Al_2O_3 sample, in accordance with the results determined by nano indentation. In the case of the co-deposited films, it can be observed how the hardness value shows a decrease compared to the deposited pure oxide layers.

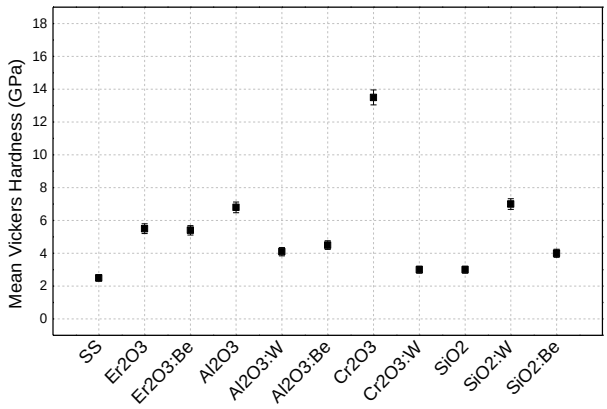

Figure 3.5. Vickers mean values (HV 0.01) based on 10 measurements and associated standard deviation [1, 9];

Figure 3.5 shows the thicknesses expressed in Vickers (GPa) for the studied configurations except for Cr_2O_3, due to the fact that the traces left by the indenter cannot be interpreted. As a result, in relation to SiO_2, the hardness increased in the co-deposition of SiO_2:W, with an average value of 7GPa, in contradiction with the results determined by nano indentation which signifies the different behavior in the multiscale analysis with the probability of the presence on the surface of some superficial structures that could express a significant influence in nanoscale measurements. For the depositions involving Cr_2O_3, the co-deposition shows a hardness reduction of up to 7 times, starting from 14GPa and going down close to the values on the substrate.

The microscratch and tribological tests were carried out to determine the adhesion of the deposited films to the substrate and the wear behavior of the deposits.

Figure 3.6 shows scratch marks produced by the Rockwell diamond tip for a predefined distance. In the case of the Er_2O_3 and Er_2O_3:Be samples, we can observe a compression fracture type model, exposing the substrate in the wake left by the indenter. For Al_2O_3 and Al_2O_3:W, bending traces were observed, which are associated with the appearance of surface stresses and which cause strong delamination by cracking [21].

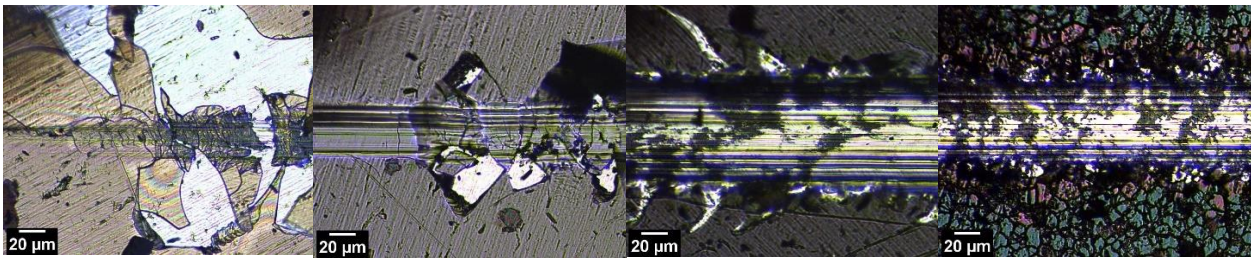

(a) Er_2O_3 – wedging spallation *(b) Er_2O_3:Be – wedging spallation* *(c) Al_2O_3 – recovery spallation* *(d) Al_2O_3:W -buckling*

Figure 3.6. Scratch marks on Er_2O_3(a), Er_2O_3:Be(b), Al_2O_3(c) şi Al_2O_3:W (d); Optical images of scratching traces [1, 9];

The traces resulting from micro-scratch measurements were classified according to the applied force values at which they appear: the first cracks, the first delamination and delamination greater than 50% of the surface of the area of interest ($0.01mm^2$). The values of the critical forces, especially those at which the total delamination of the deposits occurs, are consistent with the indentation results, with Al_2O_3 expressing the highest critical value and the highest hardness [22], followed by the Er_2O_3:Be and Al_2O_3:W samples (figure 3.7).

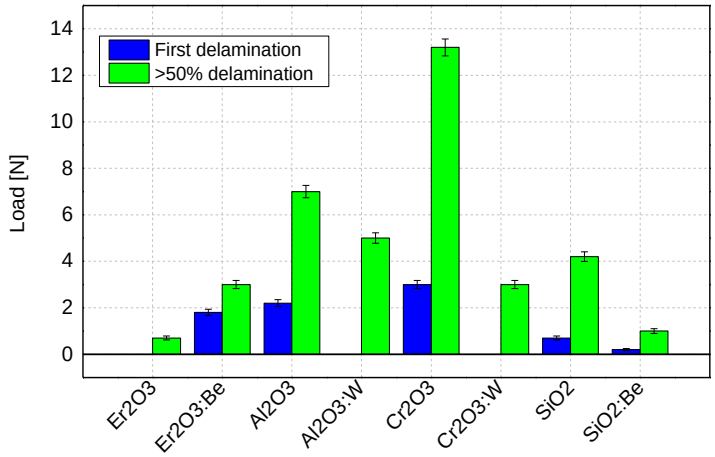

Figure 3.7. Graphs expressing the critical loads applied until the first crack, respectively until the complete delamination of more than 50% of the reference surface ($0.1mm^2$) on the systems doped and not doped with oxides;

The destruction of the layer by bending ("buckling effect") was observed for the Cr_2O_3 sample and resulted as a response to the mechanical stress generated by the indenter, where the elongated cracks perpendicular to the direction of movement of the indenter can be considered as incipient interface defects. In the case of the Cr_2O_3:W and SiO_2:Be samples that represented wedge spallation, this can be associated with the thickness of the deposited layer, where the deposition becomes brittle to further reduce the mechanical stress induced by the tip, resulting in a strong layer breaking and detachment from the substrate. The SiO_2 sample showed a recovery spallation type; this mode is associated with the elastic recovery of the layer and is dependent on the plastic deformation that evolves through isolated cracks and in the depth of the deposition.

Conclusions

Several conclusions could be withdrawn:

- Morphological characterization (SEM) and roughness (AFM) pointed out a high probability of low defects layers in the case of deposited films by TVA and RF/DC magnetron; Also, as an alternative to the SEM measurements, the X-ray computed laminography method was implemented, showing isolated defects in volume at the layer to substrate interface;
- Elemental distribution expressed as wt.% concentration was measured using EDX for oxide configurations (except SiO_2: Be), thus evaluating the stoichiometry (O and W content); while TDS data suggest that the presence of an oxide bond at the surface has led to higher desorption peak temperatures observable for N2, excepting SiO_2: Be. Moreover, defects present in the Cr_2O_3 matrix determined a significand desorption of H_2O at 400 °C;
- XPS characterized the co-deposited films as a mixture of oxidized and metallic states of the constituent elements. For the Al-based configurations, the Be presence determined the occurrence of metallic aluminum.
- Erbium oxide in both stable cubic phase and metastable monoclinic phase, respectively, were observed in pure and with W addition configurations; for pure Al_2O_3, a metastable κ-Al_2O_3 crystalline phase was observed, while the addition of W breaks the stability of κ-Al_2O_3, without significant influence on the structure;
- Modifications regarding the desorption mechanism were visible between oxide standards and oxide-metal configurations, while the desorption of O_2 is mitigated and the bound of N_2 peak is increased in the presence of W in the configuration;
- Mechanical evaluation: at nano-scale, W in co-deposition with oxides tends to lower the hardness, while Be shows a higher probability of increasing the average hardness; Tribology measurements determined that for the SiO_2 based films, the addition of W and Be leads to the increase in the coefficient of friction, while the enhancement of coating hardness is followed by the drawback of low adherence as observed for SiO_2: W configuration; adherence evaluation provided several predictable results, since the buckling mode is associated with interface defects, wedge spallation is observable for rigid coatings (e.g., Cr_2O_3: W) and recovery spallation was observable for SiO_2 in agreement with indentation results at micro-scale.
- Following multiple analysis results acquired during the implementation of the project, a limited number of samples from pure elements (i.e., W, Be, Al2O3) were validated, as well as the synthesis methods and their optimizations for which hydrogen permeation measurements were carried out using the growth method pressure and after which the permeation reduction factor was

determined. These consistent results are a starting point for future relevant improvements in the field of thin layers with permeation barrier properties applicable in the fusion reactors domain.

References

1. Lungu, M., et al., Morphological, and Mechanical Evaluation of W and Be-Al2O3 and Er2O3 Co-Sputtered Films in Comparison with Pure Oxides. Coatings 2021, 11, 1430.;
2. V. Malinovschi, A. Marin, C. Ducu, V. Andrei, E. Coaca, Valentin Craciun, Mihail Lungu, Surface and Coatings Technology, Volume 418, 2021, 127240;
3. NIST X-ray Photoelectron Spectroscopy Database, NIST Standard Reference Database Number 20; National Institute of Standards and Technology: Gaithersburg, MD, USA, 2000; p. 20899.;
4. Armelao, L. Silica-Supported Erbium-based Nanosystems: An XPS Characterization. Surf. Sci. Spectra 2004, 11, 26–32;
5. Armelao, L.; Barreca, D.; Bottaro, G. ZnO:Er(III) Nanosystems Analyzed by XPS. Surf. Sci. Spectra 2006, 13, 9–16;
6. I. Tiseanu, et al.; X-ray micro-tomography studies on carbon based composite materials for porosity network characterization, 2011, 86(9-11), 0–1651;
7. Mohammadtaheri, M.; Yang, Q.; Li, Y.; Corona-Gomez, J., Coatings, 2018, 8, 111;
8. Zhao, C., Zhao, L., Liu, J. et al., Opt. Quant Electron 2021, 53, 15
9. Lungu, M.; Cristea, D.; Baiasu, F.; Staicu, C.; Marin, A.; Pompilian, O.G.; Butoi, B.; Locovei, C.; Porosnicu, C. Surface, Structural, and Mechanical Properties Enhancement of Cr2O3 and SiO2 Co-Deposited Coatings with W or Be. Nanomaterials 2022, 12, 2870.
10. Adelhelm, C. et al., Scripta Mater. 2009, 61, 789–792;
11. Yan, D., et al., J. Appl. Phys. 2013, 114, 193502;
12. D. Hochauer et al. Surface & Coatings Technology 204, 3713–3722 (2010);
13. Makepeace, C., et al., Nuclear Materials and Energy, 2019, (19), 346–351;
14. Söderlund, E.; Reineck, I.; Rowcliffe, D. Ultralow load indentation hardness and modulus of K—and α–Al2O3 CVD coatings. J. Mater. Res. 1994, 9, 1683–1692;
15. Zhou, B., Prorok, B.C. A Discontinuous Elastic Interface Transfer Model of Thin Film Nanoindentation. Exp Mech 2010, 50, 793–801;
16. Henke L., Nagy N., Krull U. J., Biosensors and Bioelectronics, Volume 17, Issues 6–7, 2002, 547-555;
17. Vincenc Nemanič, Marko Žumer, Janez Kovač, Journal of Nuclear Materials, volume 521, 2019, 38-44
18. Journal of Nuclear Materials 521 (2019) 38e44;
19. Hydrogen în 304 steel: diffusion, permeation and surface reaction D. M. Grand*, D. L. Cummings and D. A. Blackburn 1987;
20. Tiron, V. et al., Appl. Surf. Sci. 2019, 481, 327–336;
21. Broitman, E. Indentation hardness measurements at macro-, micro-, and nanoscale: A critical overview. Tribol. Lett. 2017, 65, 23;
22. Malinovschi, V.; Marin, A.H.; Ducu, C.; Moga, S.; Andrei, V.; Coaca, E.; Craciun, V.; Lungu, M.; Lungu, C.P. Improvement of Mechanical and Corrosion Properties of Commercially Pure Titanium Using Alumina PEO Coatings. *Coatings* 2022, *12*, 29;

Project director,
(Lungu Mihail, Signature)